JOURNAL OF GEOPHYSICAL RESEARCH, VOL. 106, NO. D14, PAGES 15,215–15,232, JULY 27, 2001

Cloud coverage and height during FIRE ACE derived from AVHRR data

Patrick Minnis,[1] Venkatesan Chakrapani,[2] David R. Doelling,[2] Louis Nguyen,[1] Rabindra Palikonda,[2] Douglas A. Spangenberg,[2] Taneil Uttal,[3] Robert F. Arduini,[4] and Matthew Shupe[5]

Abstract. Cloud cover and height are derived from NOAA-12 and NOAA-14 advanced very high resolution radiometer (AVHRR) data taken over the Arctic Ocean for an 8° latitude by 30° longitude domain centered on the Surface Heat Budget of the Arctic Ocean (SHEBA) ship *Des Groseilliers*. Multispectral thresholds were determined subjectively and applied to each image, providing excellent temporal coverage during the May–July 1998 First ISCCP Regional Experiment Arctic Clouds Experiment (FIRE ACE). Mean cloud amounts were near 70% for the entire period but varied regionally from 55 to 85%. On the basis of a limited climatology of ship observations, these values appear to be typical for this part of the Arctic, suggesting that most of FIRE ACE was conducted in representative cloud conditions. A diurnal cycle of mean cloud amount was found for the domain during June and July having a range of 10% with a middle-to-late morning maximum. The AVHRR-derived cloud amounts are in good agreement with visual and radar measurements taken from the *Des Groseilliers*, except for a few subvisual and low cloud cases. Average AVHRR-derived cloudiness differ from the mean values obtained at the surface by −1 to +3%; this represents a significant improvement over previous satellite retrievals. The satellite-derived cloud heights are very accurate for most of the low cloud cases. Higher cloud altitudes are less certain because cloud optical depths were not available to adjust the temperature observed for the optically thin high clouds, and the radiating temperature of many of the high clouds is representative of some altitude deep in the cloud rather than the highest altitude level of condensate. The development of a more accurate automated algorithm for detecting polar clouds at AVHRR wavelengths will require inclusion of variable thresholds to account for the angular dependence of the surface reflectance as well as the seasonally changing albedos of the ice pack. The use of a 1.6-μm channel on the AVHRR, or other complement of instruments, will greatly enhance the capabilities for detecting clouds over poles during summer.

1. Introduction

Clouds are an important part of the Arctic climate because of their effects on the radiation budget and their role in the hydrological cycle. The First International Satellite Cloud Climatology Project (ISCCP) Regional Experiment (FIRE) Arctic Clouds Experiment (ACE) [*Curry et al*., 2000] was undertaken to obtain a better characterization of Arctic clouds and their interactions with the surface, radiation fluxes, and the atmosphere. A combination of instruments on the Surface Heat Budget of the Arctic Ocean (SHEBA) ship *Des Groseilliers* [*Perovich et al*., 1999], aircraft, and satellites furnished the measurements needed to accomplish this goal. The ship was frozen into the ice for a year and allowed to drift with the pack. The surface and aircraft data from the experiment permit the study of specific microscale or cloud-scale processes, while the satellites provide the large-scale context and spatial information. Since high latitudes are invariably remote, satellites are the most effective means for monitoring clouds over the Arctic Ocean. The surface and aircraft measurements can also serve to validate satellite retrievals and ensure their reliability.

To obtain a useful accounting of clouds in the Arctic, it is first necessary to accurately detect clouds in satellite imagery. At low and midlatitudes, satellite-observed visible (VIS) (0.65 μm) and infrared (IR) (11 μm) radiance data are used to derive cloud fraction, temperature, and optical depth. However, the extremely large and variable VIS surface albedos and diminished thermal IR contrast between low clouds and surface make the detection of clouds from satellites a difficult process in polar regions. Atmospheric conditions in the Arctic do not often meet the satellite retrieval assumptions that clouds are colder and brighter than the surface. A variety of approaches has been developed to overcome the difficulties imposed by the polar surface on satellite detection of clouds. Only a few are noted here because many of these methods have already been discussed by *Curry et al*. [1996].

The most promising techniques use solar infrared (SI) (3.7 μm) or multispectral infrared, and/or microwave data, in addition to the conventional VIS and IR data. Solar infrared is used to denote radiation in the 3.5- to 4.0-μm region because

[1]Atmospheric Sciences, NASA Langley Research Center, Hampton, Virginia.
[2]AS & M Inc., Hampton, Virginia.
[3]National Oceanic and Atmospheric Administration ETL, Boulder, Colorado.
[4]SAIC, Hampton, Virginia.
[5]Science and Technology Corporation, Boulder, Colorado.

Paper number 2000JD900437.
0148-0227/01/2000JD900437$09.00

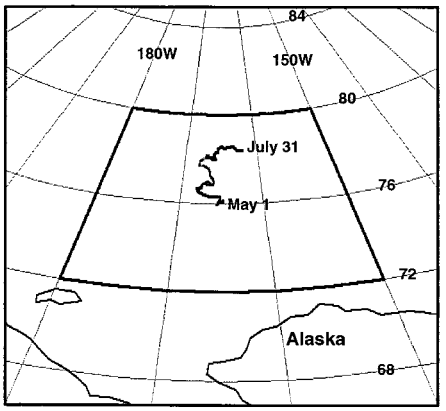

Figure 1. Analysis domain and position of *Des Groseilliers* during FIRE ACE from May 1 to July 31, 1998.

of significant contributions to the total radiance from solar reflection, as well as from terrestrial and cloud emission. *Key and Barry* [1989] used sets of fixed VIS, SI, and IR thresholds to improve the detection of clouds over polar ice and snow. The SI reflectance of the large snow grains is typically very small so that the brightness temperature difference (BTD) between the SI and the IR temperatures is also relatively small during the daytime. The initial ISCCP algorithm has recently been enhanced to use a solar-zenith-angle-dependent SI threshold in addition to the usual VIS and IR thresholds to detect clouds over snow near the poles [*Rossow et al*., 1996]. Although the use of SI data has improved detection capabilities over the poles [*Rossow and Schiffer*, 1999], the latest ISCCP approach still underestimates summertime cloud fraction by 10–50% relative to surface observations [*Schweiger et al*., 1999]. The Improved Initialization Inversion (3I) algorithm [*Chedin et al*., 1985] used to analyze the High-Resolution Infrared Radiation Sounder (HIRS) and microwave sounding unit (MSU) data, yields greater cloud fractions; these are between zero and 18% less than the corresponding surface observations during the Arctic summer [*Schweiger et al*., 1999]. One of the greatest difficulties in formulating methods for polar cloud detection has been the lack of ground truth observations. The availability of the unique SHEBA surface-based cloud fraction and altitude data set taken during FIRE ACE makes it possible to evaluate satellite-based cloud detection over the Arctic in more detail than heretofore possible.

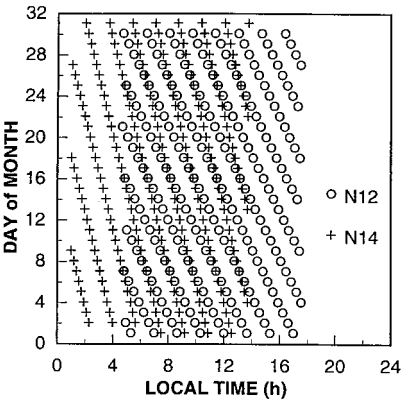

Figure 2. Nominal sampling pattern of NOAA-12 and NOAA-14 over the SHEBA ice camp during May 1998.

In this paper, a less objective approach is taken to derive cloud amount, temperature, and height from Advanced Very High Resolution Radiometer (AVHRR) VIS, SI, and IR data during the FIRE ACE period over a mesoscale to large-scale domain centered on the *Des Groseilliers* to provide an accurate quantification of these fields. These cloud properties are used to relate the FIRE ACE period to the Arctic climatology and to understand uncertainties in commonly used detection methods. Additionally, the careful examination and comparison of the subjectively derived thresholds to theoretical calculations can be used to guide the development of improved automated detection methods over snow and ice. The results of this study will be valuable for studying mesoscale cloud processes during FIRE ACE, cloud radiative effects [*Doelling et al*., this issue], and large-scale cloud microphysical properties.

2. Data

2.1. AVHRR

NOAA-12 (N12) and NOAA-14 (N14) AVHRR High-Resolution Picture Transmission (HRPT) images were collected in near real time between April 1 and August 15, 1998, from the University of Wisconsin Space Science and Engineering Center McIDAS system [*Lazzara et al*., 1999] to coincide with the FIRE-ACE observations (see http://www-pm.larc.nasa.gov/sat.gif for imagery). The images were initially centered on the *Des Groseilliers* position and consisted of 600 lines by 1300 elements to include the domain between 72°N–80°N and 180°W–150°W (Figure 1). The center point of the retrieved images varied as the ship moved until July 1 when the center point was fixed because the limited range of the satellite-receiving station in Gilmore Creek, Alaska, restricted the spatial coverage. The nominal 1-km resolution of the HRPT images increases with viewing zenith angle. As seen in Figure 2, the two satellites provide good diurnal sampling except between 1800 and 2400 LT. Only data taken during the FIRE-ACE period between May 3 and July 31, 1998, are analyzed here. The images for each overpass do not always provide complete coverage of the domain, so there is incomplete sampling over the domain. Only those images with viewing and solar zenith angles less than 45° and 85°, respectively, at the ship position were used in the current analyses. The variation of the cloud detection thresholds (see below) with viewing zenith angle precluded systematic analysis of images with larger viewing zenith angles.

A variation of the *Nguyen et al*. [1999] technique was used to normalize the calibration of each N12 channel to its N14 counterpart. The N12 counts for the visible (0.65 μm), and near-infrared (0.87 μm) channels were regressed against the corresponding N14 counts during each month of the FIRE-ACE period, using collocated data taken over the Arctic. Data were used in the normalization regressions only if they were taken within 10 min of each other and with viewing zenith θ differences no greater than 1°. Because the relative azimuth angle ψ varied rapidly with scan position, only data taken within 17° of nadir were used in the correlations.

A scatterplot of the coincident channel-1 VIS and channel-2 near-infrared (NIR) (0.87 μm) measurements, as well as the regression fits, are shown in Figure 3 for May. The standard error of the estimate in the regression fit is 3.2%. The normalization equation is

$$C_{N14} = a_0 + a_1 C_{N12}, \quad (1)$$

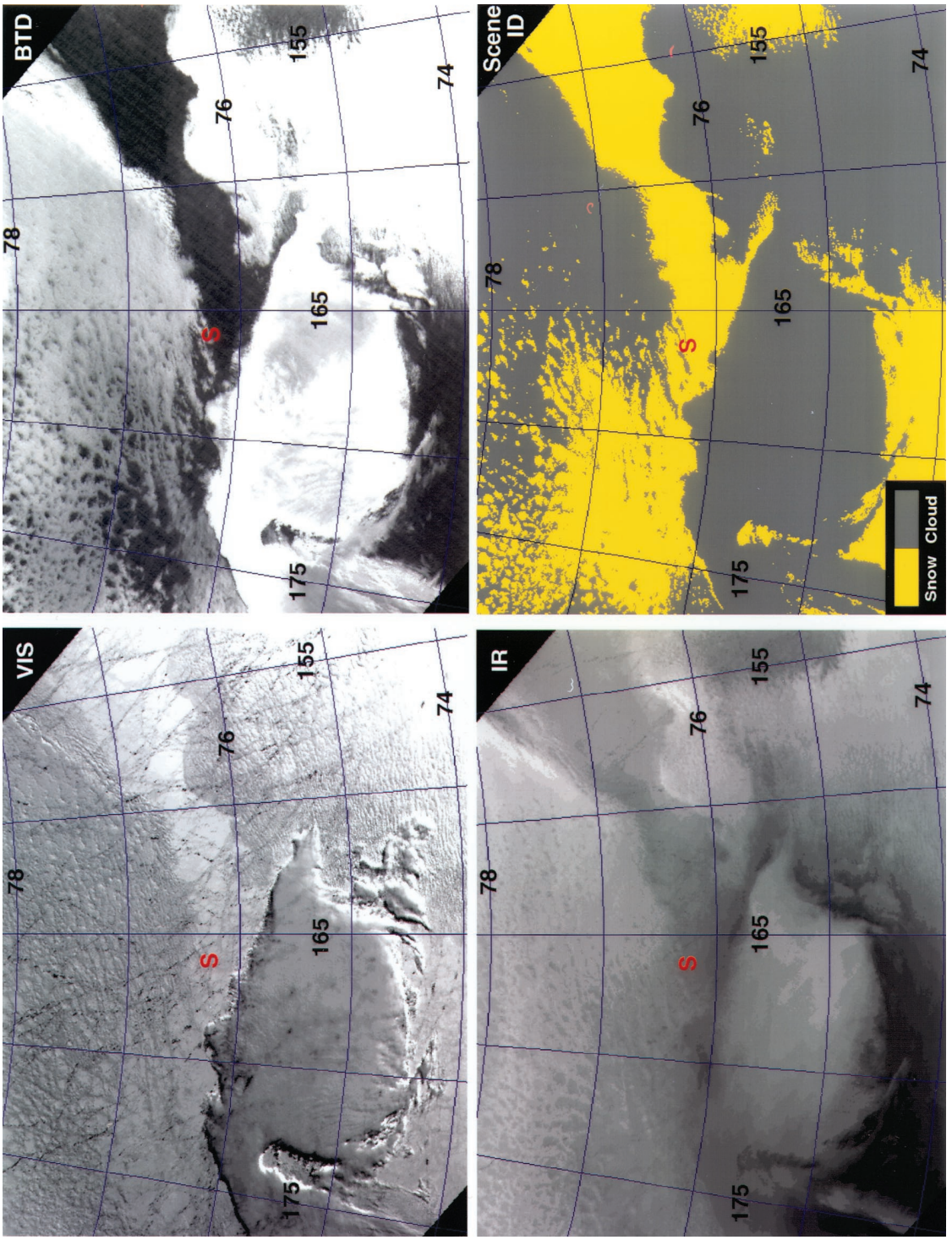

Plate 1. Visible, infrared, BTD, and scene-ID images for N12 data taken at 1936 UTC, May 19, 1998. The position of the of *Des Groseilliers* is indicated by an "S" in the images.

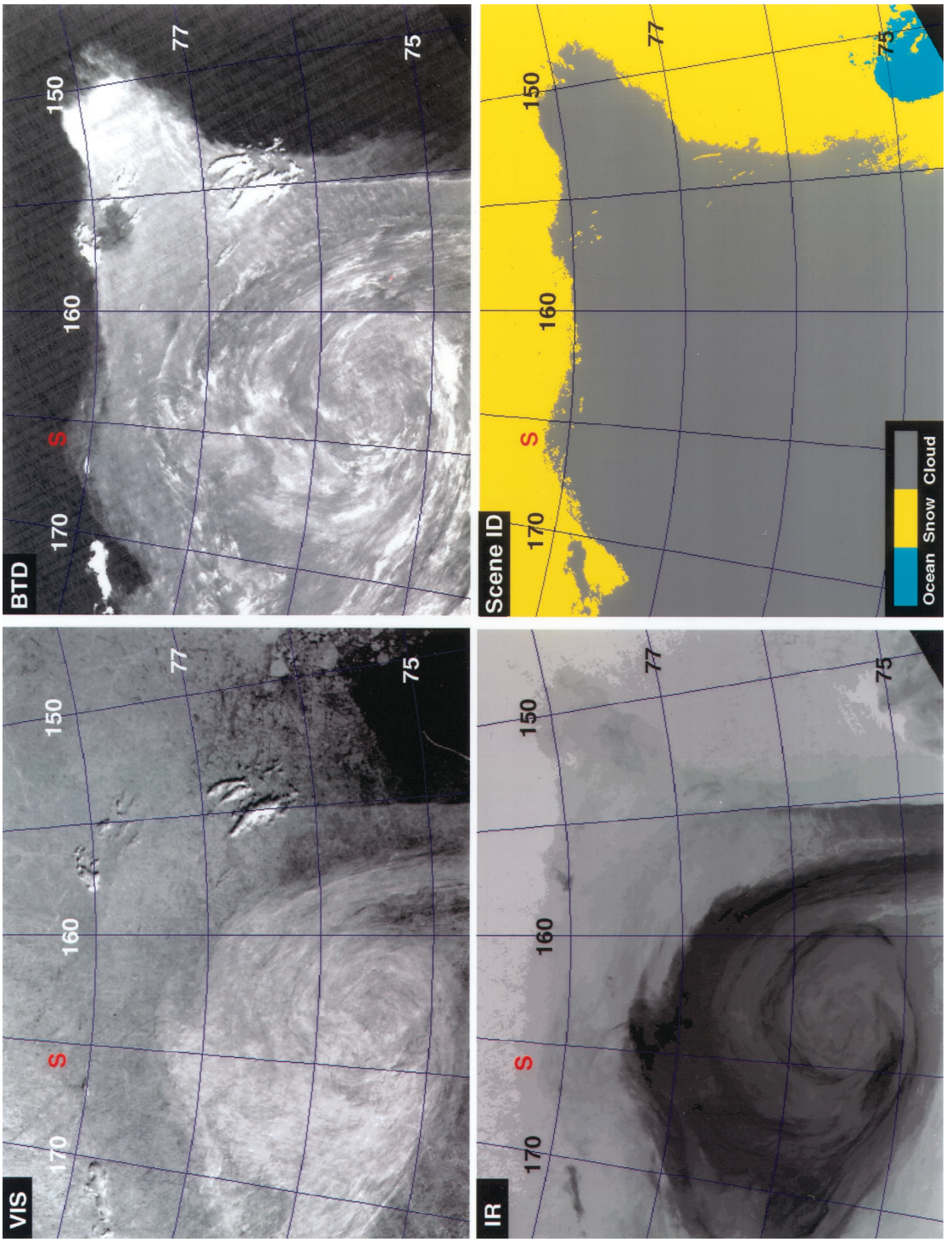

Plate 2. Same as Plate 1 except for 0251 UTC, July 21, 1991.

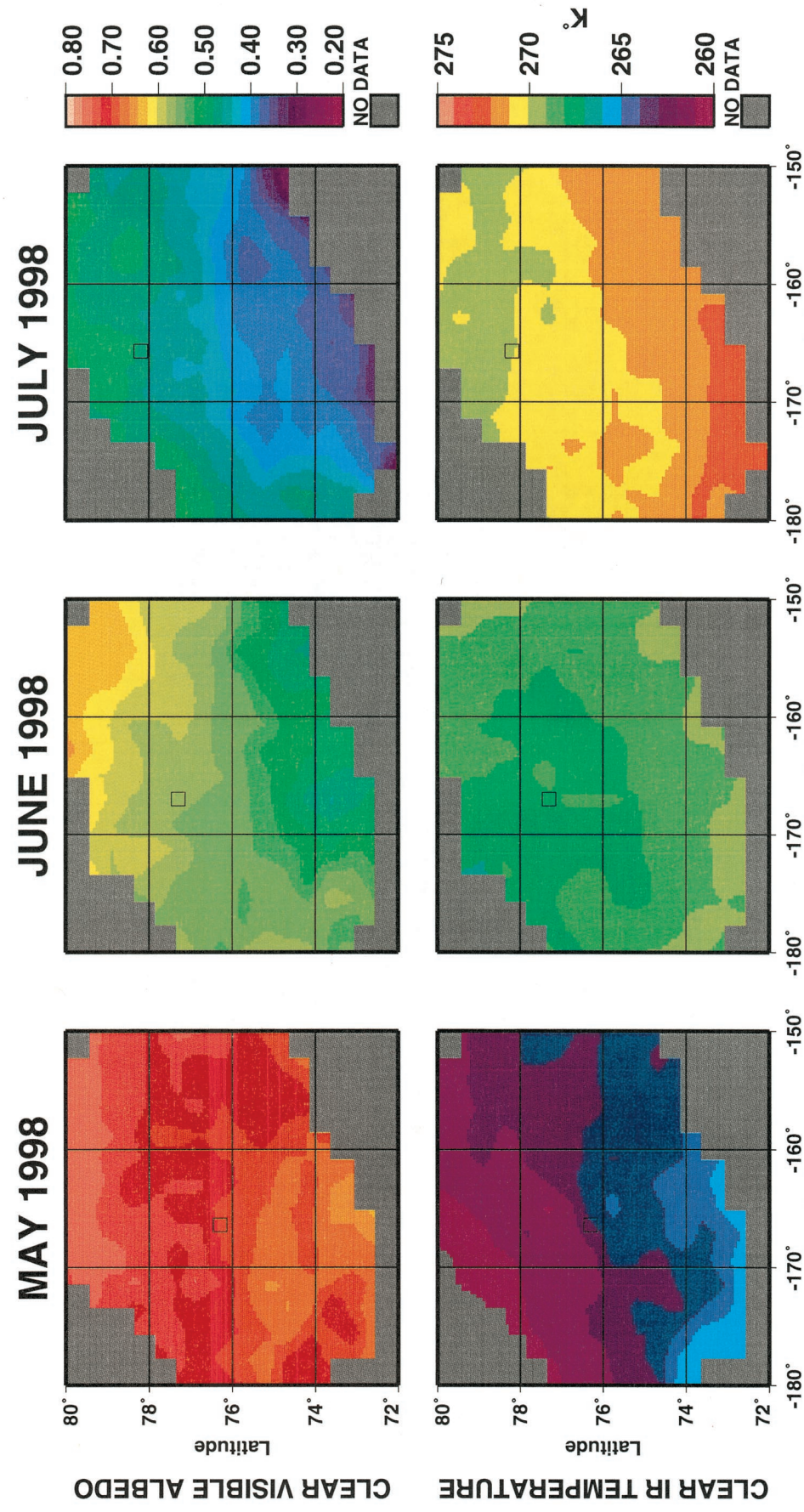

Plate 3. Distribution of mean clear-sky VIS albedos and IR temperatures derived from AVHRR data during FIRE ACE for May, June, and July 1998. Box indicates average position of the *Des Groseilliers*.

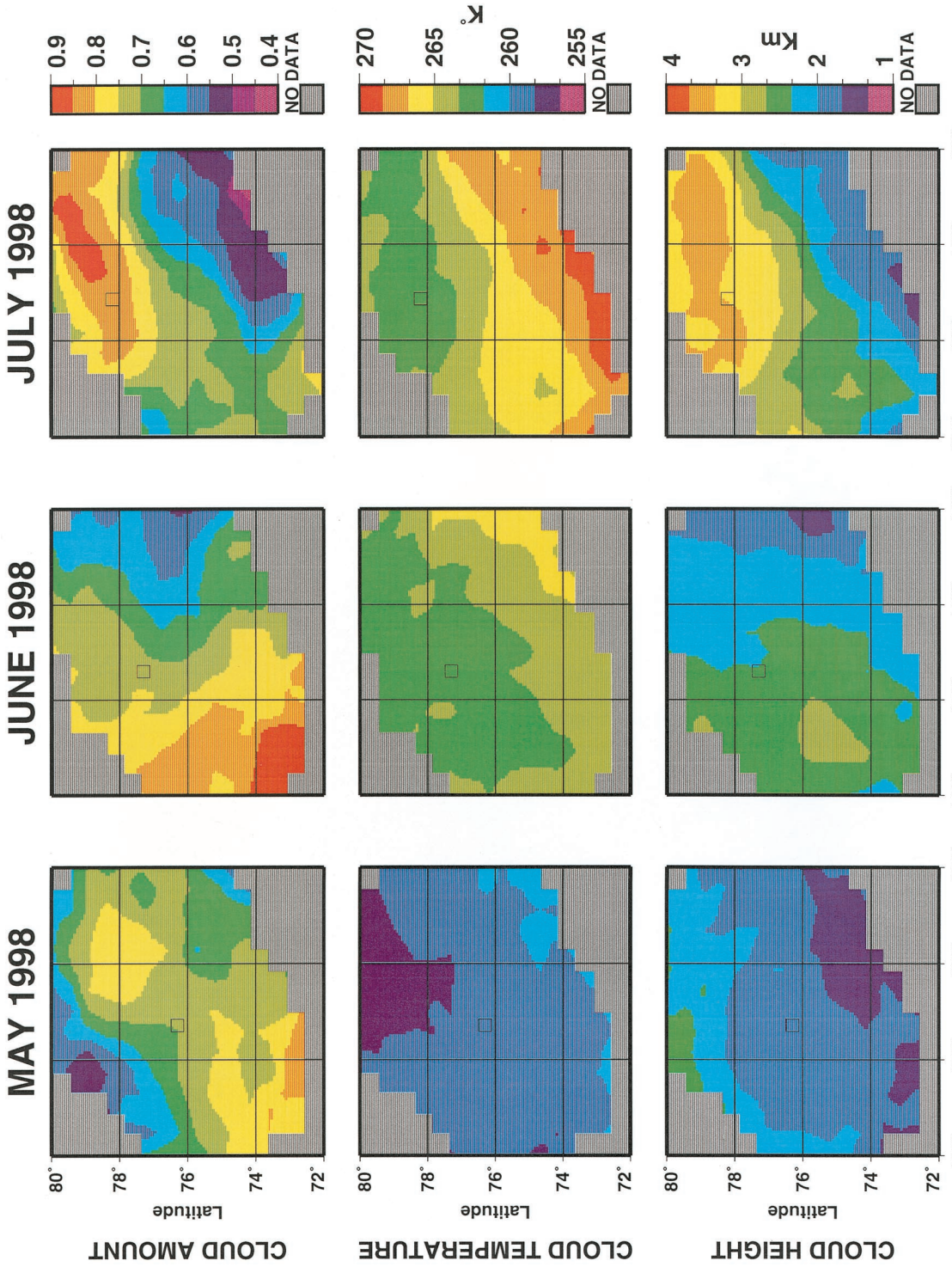

Plate 4. Distribution of mean cloud amounts, temperatures, and heights derived from AVHRR data during FIRE ACE for May, June, and July 1998. Box indicates average position of the *Des Groseilliers*.

where the 10-bit N12 and N14 counts are C_{N12} and C_{N14}, respectively. The coefficients did not vary significantly between May and July; therefore mean coefficients were used for the entire period. For the VIS channel, $a_0 = -1.8$ and $a_1 = 1.035$, $a_0 = 0.4$ and $a_1 = 1.038$ for the NIR channel. These coefficients result in normalized N12 counts that are within $\pm 0.4\%$ of the counts predicted using a different fit for each month.

The N14 or normalized N12 VIS and NIR counts are converted to narrowband radiances L_v using the *Rao and Chen* (1996 and later revisions available as of this writing at http://140.90.207.25:8080/EBB/ml/niccal1.html) degradation equations for N14. The narrowband VIS albedo is

$$\alpha_v = L_v/[D(d)\mu_0 E\chi(\mu_0, \mu, \psi)], \quad (2)$$

where D is the Earth-Sun distance correction factor for Julian day d, E is the visible solar constant for N14 (511 W m^{-2} sr^{-1} μm^{-1}), μ and μ_0 are the cosines of the respective satellite viewing and solar zenith θ_0 angles, and ψ is the relative azimuth angle. The narrowband bidirectional anisotropic reflectance factors χ from *Minnis and Harrison* [1984] were used for clear ocean and cloudy scenes, while the Earth Radiation Budget Experiment broadband bidirectional model [*Suttles et al*., 1988] is used for clear snow or ice scenes. The channel-2 albedos were computed in a similar fashion.

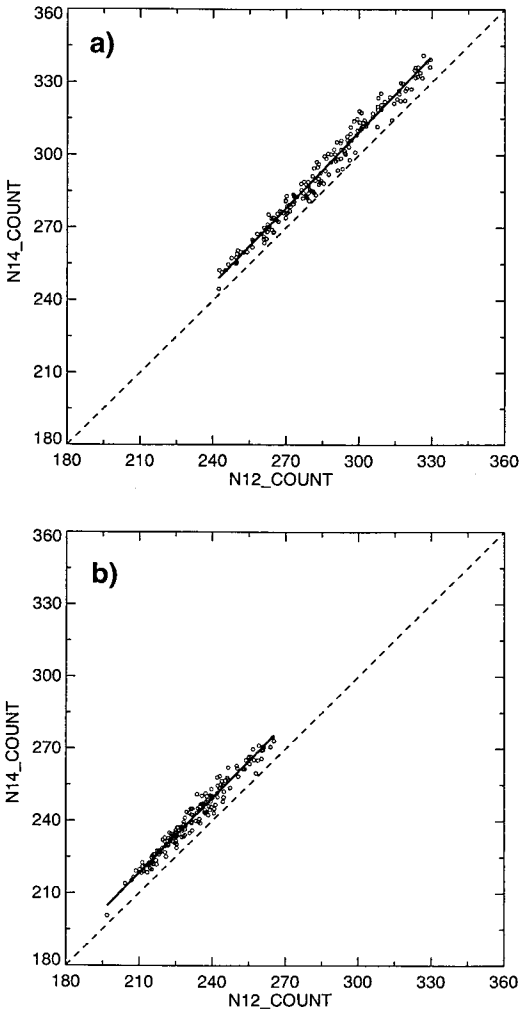

Figure 3. Scatterplot of coangled, collocated brightness counts from the NOAA-12 and NOAA-14 channels 1 and 2 for May 1998 over the western Arctic Ocean. Regression-fit lines are also shown.

The onboard calibration of the three thermal infrared channels of AVHRR should eliminate the need to normalize the N12 with N14 temperatures. However, these channels were also examined to ensure consistency. The equivalent blackbody temperatures T of N12 and N14 are related by the regression equation,

$$T_{N14} = b_0 + b_1 T_{N12}. \quad (3)$$

The mean values for the coefficients b_0 and b_1 are 5.10 and 0.983 for channel 4 (IR, 10.8 μm) and 4.60 and 0.985 for channel 5 (12.0 μm), respectively. The bias between N14 and N12 for both channels is less than 0.5 K, suggesting that there may only be a slight difference in the onboard blackbody source. This is consistent with the channel-3 (SI, 3.75 μm) temperature differences. The mean difference between N14 and N12 channel-3 temperatures for $T_3 > 245$ K is 0.8 K. Because of the solar-reflected component in channel 3, colder temperatures were not observed over the domain during this sunlit period for the matched N12 and N14 overpasses. The solar zenith angles varied diurnally from about 54° to 82° over the domain. A comparison of N12 and N14 channel-3 and channel-4 data taken during night over other areas during this time period reveals some striping in the T_3 temperature range observed during FIRE ACE. The standard deviation in the nighttime difference between T_3 and T_4 increases with decreasing temperature and corresponds to the striping evident in the channel-3 imagery [e.g., *Warren*, 1989]. At 240 K the standard deviations are 2.0 and 1.3 K for N12 and N14, respectively, and appear to decrease to less than 1 K at 250 K. This striping will affect cloud detection at very cold temperatures. The intersatellite biases in the thermal channel calibrations were not included in the analysis because they are so small.

2.2. Surface Data

Vertical profiles of temperature and humidity nominally taken close to 0000, 0600, 1200, and 1800 UTC (1100, 1700, 2300, and 0500 LT) with rawinsondes launched from the *Des Groseilliers* were linearly interpolated to the time of each overpass and are assumed to be representative of the entire domain. To simplify radiative transfer calculations and retrievals of cloud heights, these high-resolution SHEBA soundings were reduced in resolution via interpolation to 56 and 26 fixed levels, respectively. Cloud amount in octas was determined every 6 hours visually by observers at the ship. Only 80 surface visual observations out of a total of 327 for the surface and 509 from the satellite were taken within 30 min of each other. The NOAA Environmental Technology Laboratory program millimeter cloud radar (MMCR) on the ship was also used to determine cloud fraction directly overhead by counting the number of beams with returns over −50 dBz in any gate over a 30-min period centered on each overpass. A return was considered significant if its intensity exceeded −50 dBz. Cloud boundaries were determined using a combination of the MMCR, Atmospheric Radiation Measurement (ARM) Belfort ceilometer, and 523-nm Depolarization and Backscatter-Unattended Lidar data using the technique of *Clothiaux et al*. [1999].

Table 1. Mean and Standard Deviations of Cloud Detection Thresholds

Month	ΔT_{34}(CLD), K	σ, K	ΔT_{45}(CLD), K	σ, K
May	8.6	1.8	1.5	0.3
June	5.7	1.3	1.5	0.3
July	5.4	2.6	1.5	0.3

3. Scene Identification

Each image was individually examined to select a set of thresholds. The VIS, SI, IR, and brightness temperature difference (BTD) images were inspected for obviously clear regions within the domain using an interactive data analysis system. The maximum mean BTD values between channels 3 and 4 and between channels 4 and 5 corresponding to the clear areas were computed for each image to obtain the BTD thresholds. All threshold determinations for the images were completed independently of and prior to the receipt of the surface visual and radar observations. Each pixel was classified as clear ocean, snow, or cloudy using the following parameters: the VIS albedo; T_4, the channel-4 temperature; ΔT_{34}, the difference of T_3 and T_4; and ΔT_{45}, the difference of T_4 and T_5, the channel-5 (12 μm) temperature. This combination of channels provided the best separation between different scene types. The selections were made as follows: If

$$\alpha_v < 0.08\delta(\theta_0) \text{ and } T_4 > 270 \text{ K},$$

then the pixel was classified as clear ocean. The variable δ is used to account for the variation of clear ocean albedo with θ_0 and is computed here using the normalized directional reflectance model of *Minnis and Harrison* [1984]. A pixel is classified as cloudy if any of the following criteria are met:

$$\Delta T_{34} > \Delta T_{34}(\text{CLD}), \tag{4a}$$

or

$$\Delta T_{45} > \Delta T_{45}(\text{CLD}), \tag{4b}$$

or

$$T_4 < T_s - 5 \text{ K or } < T(700 \text{ hPa}) - 5 \text{ K, whichever is lowest.} \tag{4c}$$

Else, the pixel was classified as clear ocean or snow/ice. CLD refers to the clear-cloud threshold. The value of the surface temperature T_s is the first value in the sounding interpolated to the time of the image. It is assumed that over the domain the surface temperature varies by less than +5 K from the sounding value nearest the surface. This value is based on a manual inspection of the variability in the clear-sky values of T_4. Test (4a) detects most of the clouds, while (4b) identifies most remaining thin cirrus clouds. Test (4c) detects cold clouds. Except for (4c) the thresholds for each test were determined through individual inspection of each image and varied from one image to another with some dependence on the viewing and illumination angles. Table 1 lists the values for the mean thresholds and their variability for tests (4a) and (4b). The mean value of ΔT_{34}(CLD) decreases from May to July. It should be noted that these values apply only to the area and time of year used in this study.

Over snow, a VIS threshold cannot be used to determine cloudy scenes because the surface and cloudy albedos are comparable; clouds can be either brighter or darker than the underlying snow surface. In Plate 1, which shows N12 imagery taken at 1936 UTC, May 19, 1998, the clear snow VIS reflectance exceeds the cloudy reflectance. In the middle of the image the low stratocumulus clouds and the stratus deck to the south are darker than the clear surface. The cloud edges facing the Sun are the brightest pixels in the image, while the cloud edges and shadows on the north sides of the thicker stratus clouds are the darkest scenes in the image. The snow surface temperature varies by 8 K ranging from black to light gray in the IR temperature image. The locations of the clouds become more evident in the BTD image in Plate 1. In this case, test (4a) finds nearly all of the clouds as seen in the Scene-ID image in Plate 1.

An IR threshold may not always be suitable for detecting clouds over snow. In Plate 2 an extensive low-cloud deck showing some cyclonic structure is up to 7 K warmer than the surface in the IR imagery. Although parts of the cloud are brighter than the surrounding snow and ice pack, the VIS reflectance over other portions of the cloud deck is less than it is over all of the surrounding surfaces. Here again, ΔT_{34} reveals the location of the clouds (BTD image in Plate 2). Some of the apparently open water in this scene, however, is classified as a cloud because it is not dark enough to be classified as clear water. It may contain some relatively small ice floes. The identification of clouds in the daytime Arctic is considerably improved with the use of ΔT_{34} compared to the usual VIS-IR methods applied elsewhere. The relatively large particle sizes of the snow are strongly absorbing compared to the smaller droplets or crystals in clouds. Thus the snow reflects little radiation at 3.7 μm and the channels 3 and 4 temperatures are much closer over snow than for clouds. This effect is explored more in section 5.4.

When a pixel is classified as cloudy, it is assigned an altitude based on the value of T_4. In most retrievals based on VIS and IR data, it is possible to adjust the observed value of T_4 to account for the semitransparency of the clouds using the optical depth derived from the VIS channel. Optical depths were not computed in this instance because of very large uncertainties in the derived values because of the bright snow background [e.g., *Dong et al.*, this issue]. If the cloud is optically thick, no adjustment is necessary. Because no optical depths were derived here, the cloud temperature T_c is assumed to be equivalent to T_4 for all cloudy pixels. Thus the cloud temperature may be overestimated in some thin cloud conditions. The cloud-top height z_c and pressure p_c are determined by finding the lowest altitude (highest pressure) in the sounding where $T(z) = T_c$.

These procedures were applied to a total of 509 images to provide pixel-level retrievals of scene ID and cloud height, and temperature. Mean cloud amounts A_c, temperatures T_c, and heights z_c as well as mean VIS clear-sky albedo α_{cs} and clear-sky temperatures T_{cs} were computed on a 0.5° latitude by 2° longitude grid for each image. The results falling within 30 min of a given UTC hour were averaged for each month and UTC hour. For comparison with the surface observations, the results from all pixels from a given image within a 25-km radius of the *Des Groseilliers* were averaged to obtain clear-sky albedo and temperature and each of the cloud properties. *Minnis et al.* [1995] found that a region equivalent to a circle with a 50- to 100-km diameter provides the best agreement between surface and satellite cloud amounts. The mean albedo was computed

Table 2. Mean Cloud and Surface Parameters Derived From AVHRR Data for the Study Domain During 1998

	T_{cs}, K		α_{cs}		α_2	A_c, %		T_c, K		z_c, km	
Month	Ship	Domain	Ship	Domain	Domain	Ship	Domain	Ship	Domain	Ship	Domain
May	264.0	263.9	0.695	0.709	0.593	70.5	70.1	257.5	259.1	2.2	1.9
June	269.9	268.4	0.573	0.556	0.459	75.2	73.6	262.0	263.5	1.6	2.3
July	270.1	271.0	0.497	0.430	0.332	84.4	69.4	264.1	265.4	2.8	2.6

for each image and averaged using μ_0 to weight each value. The time-space averaging techniques of *Young et al*. [1998] were applied to fill in the data for missing hours and to average the values for each month.

4. Results

The distribution of mean α_{cs} and T_{cs} for each month in Plate 3 shows a gradient from north to south. T_c increases and α_{cs} decreases from spring into summer as the snow melts and the ice pack breaks up. Areas of open sea appear as the highest temperatures and lowest albedos in the southern portion of the domain. The mean clear-sky VIS albedos vary only from 0.67 to 0.76 during May. Substantial melting in the south during June increases this range to 0.48–0.65. The range during July is 0.30–0.50. Mean clear-sky temperatures vary by 6 K during May but by only 3 and 4 K, respectively during June and July. A negligible number of pixels were classified as open water during May. By July, ~8% of the domain was classified as open water.

Generally, in this paper, cloud amount, cloud fraction, cloud cover, and cloudiness are used interchangeably. Plate 4 shows the distributions of cloud amount, height, and temperature for each month. Mean cloud amount varies from 52% in the north to 83% in the south during May. The gradient in cloud fraction is nearly east to west during June with a minimum of 55%. By the end of July, the gradient reversed from the May distribution with minimum cloudiness in the southeastern corner and a maximum across the northern part of the domain. Mean cloud temperatures and heights increase steadily from May to July. Most of the clouds during May are below 2 km, while one third of the domain has an average cloud height above 3 km during July.

The monthly mean domain and ship-site cloud properties are listed in Table 2 and the mean domain channel-2 clear-sky albedos α_2. The values of α_2 are ~0.10 less than the corresponding VIS albedos. During May the AVHRR ship-site clear-sky albedos and temperatures and cloud amounts and heights are very close to the domain average. The cloud temperature is slightly less than the domain average. Except during July the mean cloudiness at the ship position is close to the average for the entire domain, as would be expected from the distribution in Plate 4.

The mean domain cloud amounts appear to undergo a fairly regular diurnal cycle during June and July (Figure 4). There is a hint of a diurnal signal during May, but it is not significant. The minimum occurs near 0300 LT, while the peak is found between 0900 and 1000 LT. The range is greatest (8%) during July when the surface albedo is lowest for the period. Because of the lack of samples between 1800 and 2400 LT (0500 and 1100 UTC), it cannot be determined if there is a semidiurnal cycle or if the cloud amount increases during the late evening.

Figure 5 shows the frequency distribution of cloud-top heights for the entire domain for each month. A quarter of the clouds are found below 500 m, while 40% of them occur below 2 km. The remaining clouds are placed between 2 and 6 km with a maximum between 2 and 3.5 km. The distributions are not substantially different from one month to the next, except that during July, more extremely low and very high (>4 km) clouds are observed than during other months. The frequent occurrence of low-level stratus and multilayered cloud systems is typical for the summertime Arctic [e.g., *Curry et al*., 1996].

5. Discussion

5.1. Cloud Amount

To determine how well these results represent true cloud conditions, it is necessary to understand how they relate to more conventional observations. Here surface observer reports

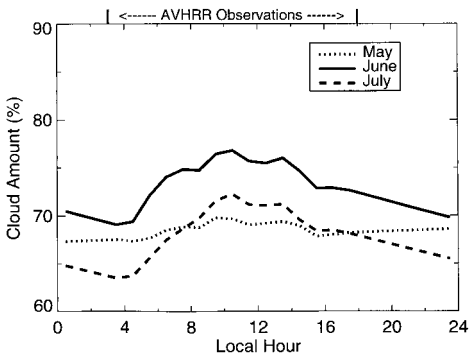

Figure 4. Diurnal variation of monthly mean cloud amount over the domain during May, June, and July 1998. Actual observations were taken between 0300 and 1800 LT. The other hours were filled by linear interpolation.

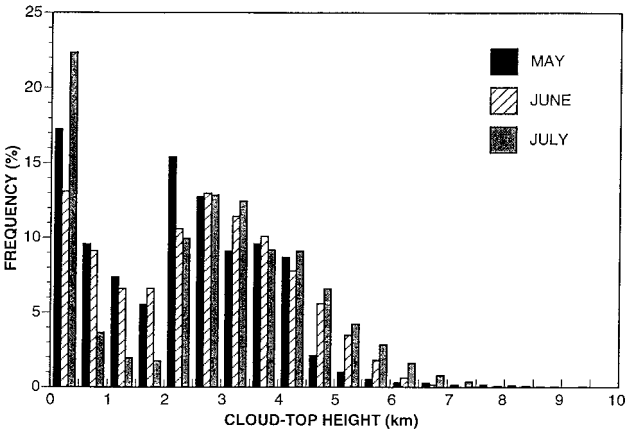

Figure 5. Distribution of cloud-top heights during May, June, and July 1998 from the satellite retrievals.

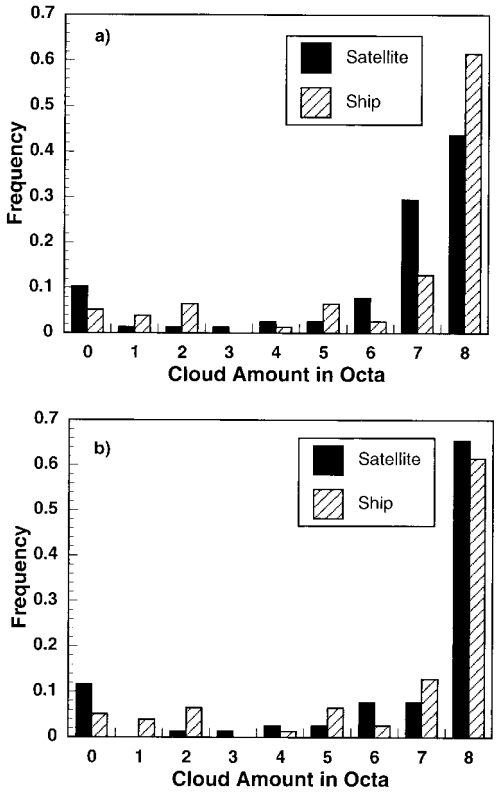

Figure 6. Frequency distribution of cloud amount from the *Des Groseilliers* surface observers and from AVHRR data within a 25-km radius of the ship during FIRE ACE.

from the ship and radar cloud fractions are compared directly with the cloud amounts derived within a 25-km radius of the *Des Groseilliers*. Comparisons of surface and satellite cloud amounts are subject to some difficulty because of scale differences, surface observer subjectivity, the low resolution of surface cloud amount digitization (octas), and the limited resolution of the satellite imager pixels. Discussion of the problems affecting these types of comparison may be found in the works of *Henderson-Sellers and McGuffie* [1990], *Minnis et al*. [1995], and in some of the references therein. Despite such problems, it is generally expected that both approaches should yield very similar mean cloud amounts for a significant number of samples. The mean and standard deviation of the difference between these 80 surface visual observations and the satellite results are 0.020 and 0.123, respectively. The bias represents only a 2.6% relative underestimate of the surface observations, while the rms difference is equivalent to a one-octa uncertainty in the surface observations. If a 3-hour window is used, the bias and root-mean-square (rms) difference increase to 0.038 and 0.144, respectively, for 327 points. For clouds as low as those in this domain, a 25-km radius may be too large to accurately represent the distance observed from the surface because the low clouds foreshorten the horizon.

The average cloud fractions from the surface observers for each month are 73.3, 71.5, and 80.7% for May, June, and July, respectively, if obscured observations due to drizzle, snow, and fog are not included. If it is assumed that these obscured cases are actually overcast, then the respective monthly mean *Des Groseilliers* cloud amounts rise to 76.3, 76.0, and 86.7%. Thus the mean AVHRR-derived cloud amounts over the ship (Table 2) are in good agreement with the surface observations for June and July. However, it appears that the satellite analysis underestimates the May total cloud cover by 3–6%. Considering the range in observations for the entire period due to the unknown cases, the satellite cloud amounts are either 1.3% too high or 3% too low relative to the surface reports.

Another way to evaluate the satellite results is to determine if the distributions of cloud amounts from the two data sets are comparable. The AVHRR cloud amounts were binned according to octas to match the cloud amounts observed from the surface. In the first comparison the AVHRR cloud fractions are defined according to the standard observing rules. No scenes could be classified as clear (zero octas) if only one pixel was classified as cloudy. Conversely, a scene could be classified as overcast (8/8) only if there were no clear pixels. Between clear and overcast, 1/8 corresponds to $0 < A_c \leq 18.75\%$, 2/8 is $18.75\% < A_c \leq 31.25\%$, and so forth, to 7/8 is $81.25\% < A_c < 100\%$. The larger ranges for 1/8 and 7/8 are used because only seven intervals are available. The satellite-surface comparison using this definition (Figure 6a) shows that the surface observer sees more overcast and fewer clear skies than the satellite, while the satellite obtains more mostly cloudy and fewer partly cloudy cases according to the octa definitions. The surface observer also sees twice as many 7/8 cloudy skies as the satellite and less than half the amount of clear skies.

If it is assumed that 1/8 cloud fraction corresponds to $12.5\% \pm 6.25\%$, 2/8 to $25\% \pm 6.25\%$, and so forth, then clear and overcast would correspond to $A_c < 6.25\%$ and $A_c > 93.75\%$. The histograms were recreated using these definitions and plotted in Figure 6b, which shows that the frequency distributions of cloud amounts from the satellite and surface data are in much better agreement. Examination of some of the cases indicates that the surface viewer detects partly cloudy conditions in some optically thin cloud cases where the satellite sees little or no cloudiness. As indicated below, the radar detects overcast conditions in these same cases. These conditions may explain the satellite underestimates during May relative to the ship.

To minimize noise in the radar-derived cloud amounts, cloud fraction was computed by using only those cloud returns

Table 3. Frequency of Cloud Amounts in Percent From Radar, AVHRR, and Surface Observations at the *Des Groseilliers*, May–July 1998

Radar A_c, %	AVHRR A_c, %				Ship Observer A_c, %			
	0–15	15–50	50–85	85–100	0–15	15–50	50–85	85–100
0–15	7	1	0	1	9	4	0	1
15–50	1	1	1	1	1	1	1	1
50–85	1	1	1	1	0	0	2	2
85–100	5	5	12	61	1	5	12	60

Table 4. Mean and Standard Deviations of ISCCP D2 Cloud Properties for 1983–1994 for 72.5°–80.0°N and 130°–170°W

	May		June		July	
Property	Mean	σ	Mean	σ	Mean	σ
A_c, %	58.9	8.9	55.1	7.0	56.8	9.5
p_c, hPa	710.2	31.9	714.5	14.5	650.0	20.4
T_c, K	257.0	2.1	261.7	1.1	262.0	1.8
α_s	0.83	0.02	0.74	0.03	0.61	0.03
T_{cs}, K	262.2	1.3	269.5	0.7	272.5	1.2

that persisted more than 5 min in the radar image and by eliminating all times when there were a few minutes of data dropout. The results are compared with satellite and surface-observer cloud-amount frequencies for four range categories in Table 3. There is excellent agreement between all three data sets for most clear and overcast conditions. The greatest discrepancies occur in the last row of the table where the radar detects an overcast scene, while the satellite and surface observer see significantly less cloudiness, 22 and 18% of the time, respectively.

Examination of the radar data reveals that in many of these cases the radar detects a physically thick but apparently optically thin high-cloud layer or some diamond dust at low levels which produces returns with intensities smaller than −25 dBz. In a few cases, higher intensities occur periodically within the continuous cloud deck, as seen in Plate 5 for May 21. The surface observer detects some clouds in these instances but does not interpret the layer as overcast because of some very thin parts. The satellite image for 1628 UTC in Plate 6 shows the variability in these high clouds. Shadows cast by the almost linear thick portions of the clouds are evident in the VIS image. In the IR image, the areas between the obvious clouds appear to be clear. Inspection of the BTD image in Plate 6, however, reveals more high cloudiness than is seen in the IR image, but many of the ΔT_{34} values are only ~3 K, well below the cloud detection threshold. In this case, the cold cloud test finds most of the cloud layer seen by the radar because T_4 is 10 K colder than the surface. The observer on the ship cannot see most of these clouds, and they are nearly transparent in the IR data. Thus it is assumed that they are subvisual clouds with extremely small optical depths (<0.1). From these subjective and objective comparisons it is concluded that except for subvisual clouds, the current analysis of AVHRR data yields cloud amounts that on average are within 3% of those seen from the surface for clouds.

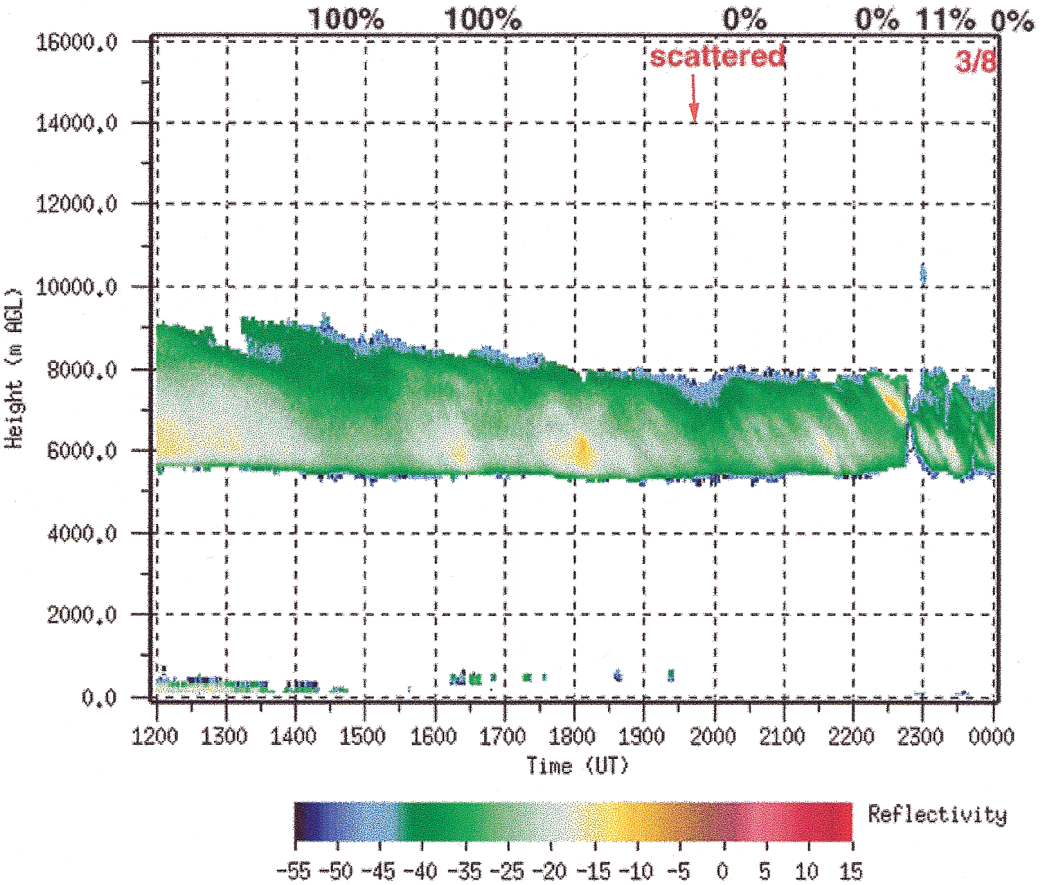

Plate 5. MMCR image from the *Des Groseilliers* from 1200 to 2400 UTC, May 21, 1998. Percentages at top are satellite-derived cloud amounts. Fraction in red is surface-observed cloud amount. Cloud amount was not given quantitatively at 1945 but was indicated as scattered.

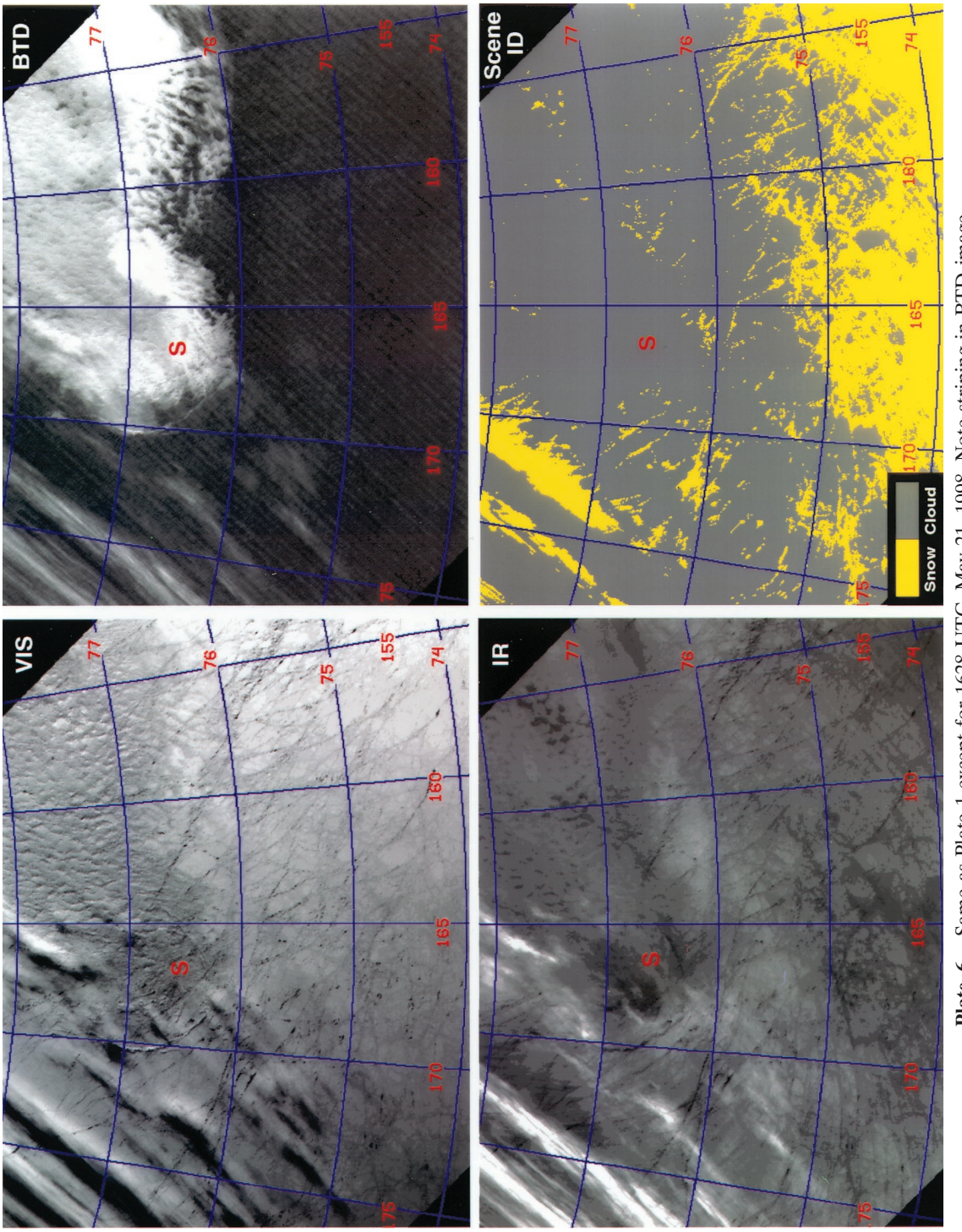

Plate 6. Same as Plate 1 except for 1628 UTC, May 21, 1998. Note striping in BTD image.

The diurnal variation in mean cloud amount from the ship observations is characterized by a 7% range during each month. During May and June the maximum occurs between 0700 and 1300 LT, a period similar to that for the domain maxima seen in Figure 4. During July, however, the ship observations show a minimum at 0700 LT and a maximum at 1900 LT. The satellites did not observe the domain after 1800 LT, so the linear interpolation used to fill in missing hours would have missed the maximum. The difference between the satellite and the surface observations for July, however, is most likely due to the ship position. During May and June the ship observations were very close to the domain averages. However, during July the ship was farther north, and the cloud characteristics were different from the domain averages. Another source of discrepancy is the sparse sampling from the surface. The four local times of observation do not provide a sufficiently detailed picture of the diurnal cycle.

The reasons for the diurnal cloud variations observed for the domain are not obvious. During May the absorption of solar radiation, reflected in the slight mean diurnal range in the skin temperature evident in the mean diurnal range of $\sim$2.5 W m^{-2} in the clear-sky longwave radiative flux [*Doelling et al.*, this issue], may provide some sensible heat for convection. The mean May surface air temperature ranges from $-10.2°$ to -7.3°C at the ship indicating that a significant amount of sensible heat is being transferred from the surface. During June and July the mean diurnal ranges in surface air temperature are 1°C and 0.4°C, respectively, while the mean diurnal variations in clear-sky longwave flux are negligible. The mean relative humidities vary by 6, 3, and 2% during May, June, and July, respectively. Thus the transfer of sensible heat diminishes as the apparent diurnal cycle in cloud fraction increases and would not support more convection during July than during May. It should be noted again, however, that the ship is less representative of the domain average during July than during May, so the diurnal cycle in air temperature may be greater than measured by SHEBA. More detailed analysis of the diurnal variations of the thermodynamic variables in the boundary layer are needed to understand the diurnal cycle in low-level cloudiness.

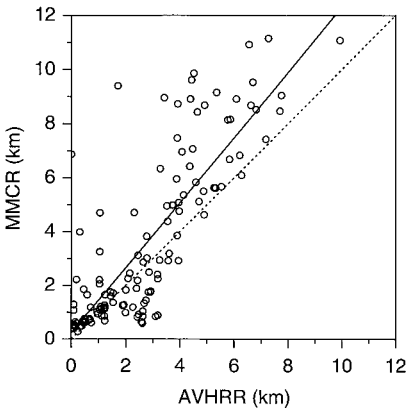

Figure 7. Scatterplot of cloud-top heights from the *Des Groseilliers* MMCR and the AVHRR retrievals during FIRE ACE. The regression-fit (solid) and agreement (dashed) lines are also plotted.

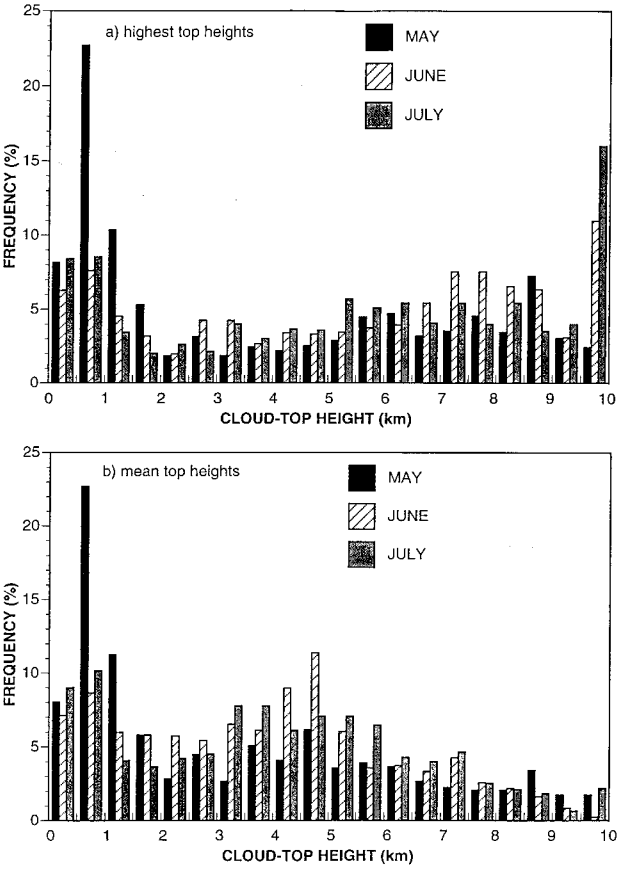

Figure 8. Histograms of cloud-top heights from the SHEBA MMCR during May–July 1998.

5.2. Cloud Top Altitude

Cloud-top heights from AVHRR were matched with the radar data for all single-layer cloud cases with $A_c > 90\%$ to provide a clean comparison. The results plotted in Figure 7 show that the cloud top heights from the AVHRR retrieval agree very well for many of the low-cloud cases and for some of the higher clouds. Most of the high-cloud tops are underestimated by the satellite retrievals by an average of 2 km, presumably because these clouds are optically thin and no emissivity corrections were applied. The mean altitude difference between the two retrievals is 0.8 km with a standard deviation σ of 1.8 km. Most of the higher clouds are also geometrically thick and optically thin so that the mean radiating temperature is probably representative of some level within the cloud rather than the highest altitude of condensate. Thus corrections for semitransparency may not bring the satellite and radar cloud tops into complete agreement for these cases. For low clouds with top heights below 2 km the satellite retrieval overestimates cloud-top height relative to the radar retrieval. These clouds appear slightly colder than the coldest temperature under the near-surface inversion layer and are placed 2 km higher. Because the SHEBA soundings were reduced in resolution, some of the thinner inversion layers may have been eliminated. Thus the cloud would be placed higher in the atmosphere where the temperature occurs again. The reduced resolution soundings are similar to the type of resolution that would be available during a routine operational analysis of clouds. Thus the cloud height errors due to vertical

profile resolution seen here will generally be encountered in any operational cloud height retrieval.

Cloud layering may also affect the determination of cloud heights. For example, if it assumed that a high thin cloud occurs over a thick cloud, then the satellite will see some of the radiance from the thick cloud through the thinner one. The resulting cloud temperature will be somewhere between the radiating temperatures of the two clouds. To see how such an effect would alter the cloud height distribution, cloud height histograms from the radar were constructed in two ways. In one case, the highest-cloud-top height was counted whether it occurred with a cloud below it or not. Thus in a multilayer cloud, only the highest cloud-top height counted as one occurrence. In the second case, the cloud-top heights were averaged for multilayer clouds. The results are shown in Figure 8. In Figure 8a the histogram for individual clouds shows a high frequency of clouds above 5 km. The averaged cloud-top heights in Figure 8b are more frequent between 3 and 6 km with far fewer clouds occurring at altitudes above 6 km. This latter histogram is more like that in Figure 5 than in Figure 8a. The satellite, however, detects far fewer clouds above 6 km than either averaging method. Clearly, both semitransparency and overlapped clouds must be taken into account to achieve accurate remotely sensed cloud heights from AVHRR data.

5.3. Climatology

Few long-term surface observations of cloud amounts are available from the Arctic, although some average values for 1952–1981 are reported for a few Arctic locations in the surface cloud observation atlas of *Warren et al*. [1988]. Their mean total cloud amounts for the area between 140° and 165°W and 75° and 87°N for that period are 73, 81, and 85% during May, June, and July, respectively. While the seasonal trends are similar to those seen in the AVHRR observations, the magnitudes are 5–10% greater than the domain averages in Table 2 and close to the magnitudes derived from the *Des Groseilliers*.

The ISCCP satellite observations probably constitute the longest, recent record of cloud amounts for this area. Average cloud properties were computed using the D2 products from May and June 1984 to 1994 and from July 1983 to July 1994 for the area encompassed by 72.0°–80.0°N and 130°–170°W (see Table 4). The cloud amounts are between 15 and 30% less than those determined from the earlier surface climatology and do not exhibit an increase as the summer proceeds. This difference between the ISCCP cloud amounts and the surface climatology is similar to the differences reported by *Schweiger et al*. [1999] for a different portion of the Arctic using ISCCP D2 and ship data taken during 1990. If it is assumed that the cloud variability in the ISCCP data set is a true reflection of the interannual variations that would be observed from the surface, then the *Des Groseilliers* averages are within one ISCCP standard deviation of the means from *Warren et al*. [1988]. Thus it can be concluded that the mean cloud amounts during FIRE ACE are typical for that part of the Arctic even though the extent of the ice pack in the Beaufort and Chukchi Seas reached a record minimum during July 1998 [*Maslanik et al*., 1999].

The surface albedos from ISCCP can be compared with those from the current analysis by correcting the domain TOA VIS albedos in Table 2 for ozone absorption and Rayleigh scattering. The TOA VIS albedo was computed as a function of Lambertian surface albedo using the adding-doubling model of *Minnis et al*. [1993] at 0.65 μm. The computations assume an ozone optical depth of 0.03 and account for Rayleigh scattering. Aerosol effects were not included so the albedos would be directly comparable to the ISCCP values, which were derived without including aerosol effects. The domain values in Table 2 yield surface albedos of 0.82, 0.72, and 0.60 for May, June, and July, respectively. Except in June, when the current value is 0.05 less than the ISCCP result, there is good agreement between these results and the 11-year means, suggesting that the composition of the surface (i.e., snow, ice, ponds, etc.) is fairly typical for this domain. Inclusion of aerosols in the surface albedo retrieval would increase or decrease the derived values depending on the solar zenith angle range and the type and concentration of the aerosols. For example, using the adding-doubling model for $\theta_0 = 75°$ and 45°, a clean maritime aerosol [*Hess et al*., 1998] with an optical depth of 0.1 would produce TOA VIS albedos of 0.675 and 0.715, respectively, for a surface albedo of 0.80. An Arctic aerosol containing more soot and mineral dust [*Hess et al*., 1998] for the same conditions would yield TOA albedos of 0.591 and 0.656, respectively. These results can be compared to the corresponding aerosol-free results of 0.664 and 0.716. Because of no information about the aerosol types and concentrations during FIRE ACE are currently available and the sensitivity of the calculations to aerosol type, no attempt was made to account for the aerosols in estimating surface albedo.

During May the domain clear-sky temperature is 2 K greater than the ISCCP mean, a value that is slightly larger than the standard deviation. During June the FIRE ACE T_{cs} is within the interannual variation derived from the ISCCP data. However, during July, T_{cs} is 2.4 K less than the ISCCP mean, a difference equal to two standard deviations.

Cloud amounts are 11, 19, and 13% greater in this study than the corresponding ISCCP means for May, June, and July, respectively; these differences are discussed below. Average cloud-top pressures and temperatures are 40 hPa and 2 K greater, respectively, from the current analysis than from the ISCCP mean for May. This difference is typical of the values during the entire period. The value of T_c is within 1σ of the ISCCP mean only in May. The temperature and pressure differences may be due either to the detection of more low clouds here or due to the lack of an optical depth correction. It is not clear how often optically thin clouds were detected by the ISCCP in this area. Overall, both the clear and the cloudy temperatures are 2 K warmer than that observed by ISCCP, suggesting either an IR calibration difference or greater-than-usual warming during May. Only the cloud temperatures were 2 K warmer than the ISCCP average during the other months.

The ISCCP D1 data set provides 3-hourly cloud parameters on a 250-km scale. Over the Arctic, past NOAA satellites have taken data at all hours of the day. The 3-hourly averages between 1984 and 1994 have a maximum at 1000 LT (2100 UTC) and a minimum around 2200 LT. The ranges vary from 19 to 34% for the 3 months. The spatial coverage between 0600 and 1200 UTC is much less than that for other times, so the averages may not be so representative at those hours. For the same hours sampled in this study, the diurnal ranges in the ISCCP cloud averages vary between 8 and 10%, similar to the values found here. Thus both the phase and the range in mean cloud amount during FIRE ACE is consistent with past measurements and the contemporaneous ship observations.

5.4. Current Versus ISCCP Analyses

From comparisons to surface observations, it has been shown that the retrieval method applied here yields more ac-

curate cloud amounts than obtained using the ISCCP D version for cloud detection [*Rossow et al*., 1996]. Both techniques used the same general approach to cloud detection using AVHRR data. The difference primarily relies on the selection of threshold values and the input data used to set the thresholds. ISCCP uses a fixed BTD threshold of 8 K or the difference that is equivalent to a SI reflectance of 0.055 for all cases, while the current method used subjectively determined BTD thresholds that vary depending on the scene. The approach used here cannot be applied in an operational mode because the volume of data precludes a subjective analysis. Additionally, the ISCCP relies on a composite map gathered over several weeks to determine the clear-sky temperatures for IR threshold determination. The compositing approach provides a highly uncertain clear-sky temperature [e.g., *Schweiger et al*., 1999] in the Arctic because of the initial difficulty in screening clouds to find clear scenes. The current analysis used relatively high temporal resolution soundings to provide temperatures at the surface and 700 hPa to set the IR threshold. The ISCCP also does not have the luxury of having the high-resolution soundings available during FIRE ACE.

The sounding problem could be mitigated to some extent by employing an IR threshold corresponding to some selected altitude above the surface using the temperature from the ISCCP TOVS sounding or some other atmospheric profile, as used here. The variability of the SI threshold may be taken into account by using a SI bidirectional reflectance model of the snow surface like that employed by *Han et al*. [1999] for the VIS channel. An example of such a model is shown in Figure 9a. The curves in this figure are the results of reflectance calculations from an adding-doubling model [*Minnis et al*., 1993] for an ice cloud with an optical depth of 1000 and temperature of 260 K. Optical properties for a hexagonal ice column 750 μm long and 160 μm wide [*Minnis et al*., 1998] were used to simulate large snow crystals. Over the range of solar zenith angles in the Arctic the SI reflectance remains below 0.02 for all azimuth angles but direct forward scattering and for $\theta < 60°$, except when $\theta_0 = 82.1°$. Most useful data are taken at $\theta < 60°$. The corresponding BTD values shown in Figure 9b vary from 2 to 6 K for the assumed surface (cloud) temperature for $60° \leq \theta_0 \leq 82.4°$. These values are very close to the mean values computed from the clear scenes in May. The mean domain value during May was 4.4 K for an average value of θ_0 of 71.1°. It ranged from 2.8 to 5.7 K depending on θ_0. The empirical thresholds suggest that the variation in the reflectance is nearly as large as the values themselves.

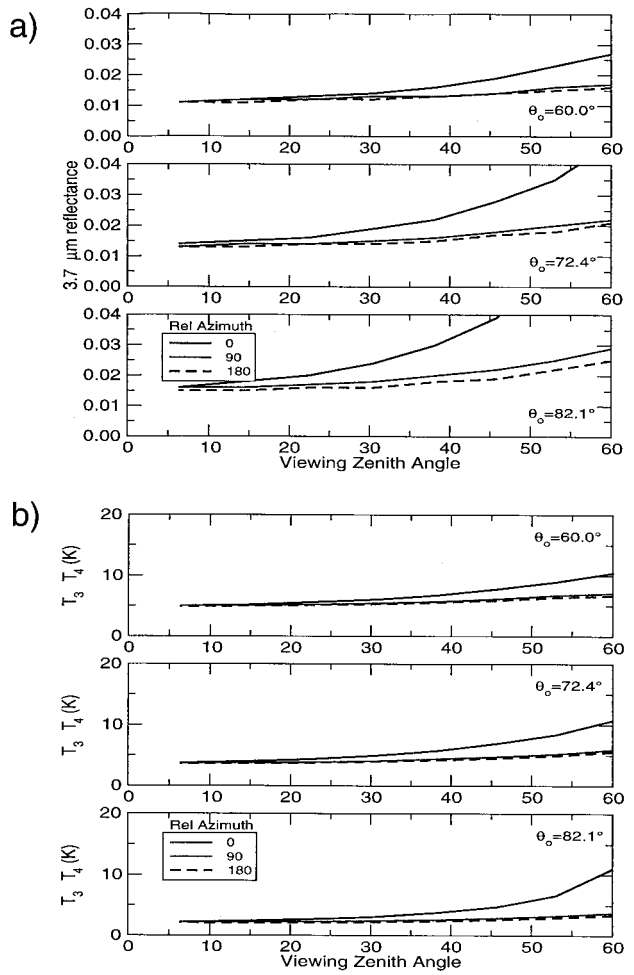

Figure 9. Simulation of snow (a) 3.75-μm reflectance and (b) ΔT_{34} from theoretical calculations using a hexagonal ice crystal cloud with an optical depth of 1000 at $T_c = 260$ K.

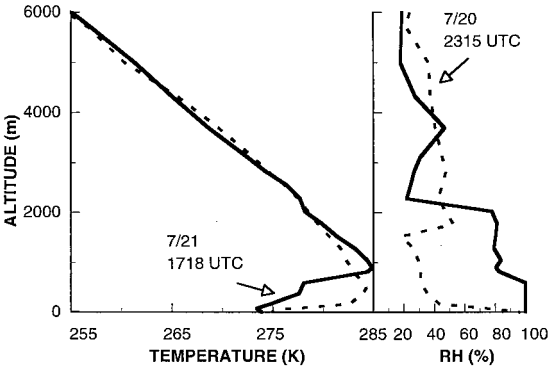

Figure 10. Temperature profiles from rawinsondes launched from the *Des Groseilliers* during FIRE ACE, taken before (left) and during (right) times when clouds passed over the ice camp.

The reflectances in Figure 9a vary with the angles, indicating that biases in cloud detection will depend on the viewing and illumination angles if a fixed reflectance threshold is used. This variability is the primary reason why the viewing zenith angle was limited in this study; a single threshold was used for each image. Because it corresponds to more than twice the current values in Table 1, the ISCCP BTD threshold would probably classify more cloudy pixels as clear than the present method. As the surface temperature rises, the average BTD for clear snow will decrease because of the extremely nonlinear variation of radiance with temperature at 3.7 μm. This change is consistent with the decreasing thresholds during June and July in Table 1. While a method using a model like that in Figure 9a may be more realistic, it may have difficulty accounting for reflectance variability when the surface becomes slushy or contains ponds that reduce the albedo as seen in the VIS channel during June and July (Table 2). Thus any model applied in an automated fashion may need to be more sophisticated than the simple one-crystal calculation demonstrated here.

5.5. Warm Clouds

Most of the clouds in Plate 2 are warmer than the surface; a few are of the same brightness or are darker than the surface

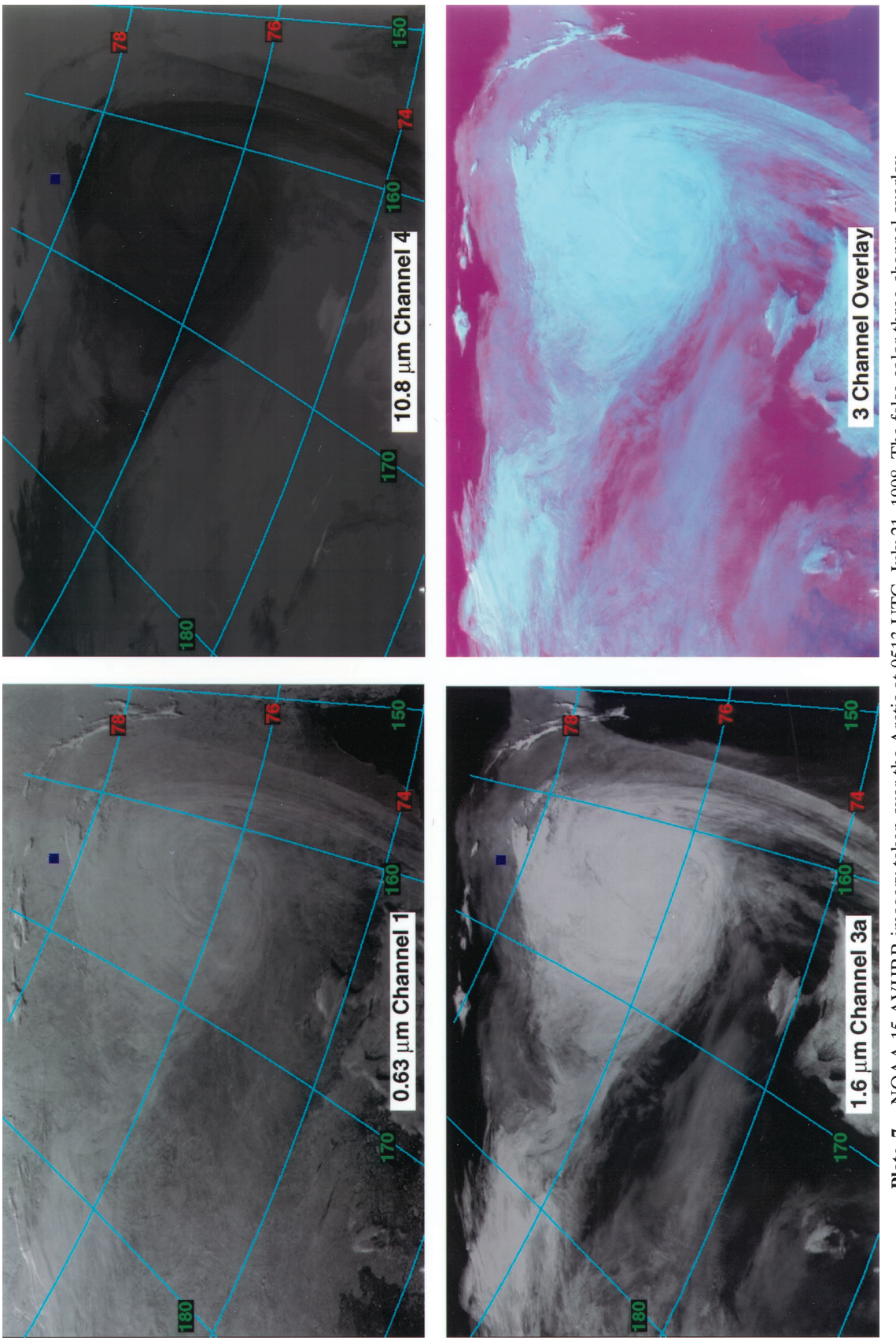

Plate 7. NOAA-15 AVHRR imagery taken over the Arctic at 0513 UTC, July 21, 1998. The false color three-channel overlay (red = VIS, green = 1.6 μm, blue = IR) was created using histogram equalization to enhance differences among snow (pink), clear water (dark blue), thick water cloud (white), ice clouds (light blue/gray), and thick clouds over various backgrounds.

in the VIS channel. Without the BTD technique, it would be extremely difficult to detect all of these clouds even with a sounding approach like the 3I method because of the obviously strong inversion associated with this warm cloud. Figure 10 shows two soundings, one prior to the passage of this warm cloud deck over the SHEBA camp at 2315 UTC, July 20, and another at 1718 UTC, July 21, when the cloud deck was above the site. The thinner, lower clouds reached the camp around 0500 UTC and had thickened to 800 m by 1200 UTC. The cloud deck took ~18 hours to pass over the camp. The first sounding shows a strong inversion from the surface to 400 m. The relative humidity RH at the surface is nearly 100%. A humidity decrease then occurs at 1500 m, while the temperature lapse rate is fairly constant above 400 m. After the cloud deck rolled in, the atmospheric structure became more complex with an inversion base at 100 m above the surface, another change in lapse rate at 300 m to a much stronger positive lapse rate to 800 m, the top of the boundary layer inversion. The air is saturated up to 600 m. Relative humidity decreases to 80% at the top of the inversion, then remains constant up to 2000 m. The radar places the cloud top at 800 m and the base near the surface.

This entire cloud exists in air that is very stable and moist with a top that is 10 K warmer than its base. This structure suggests that it is similar to a deep advection fog produced by warm air from the south that was moistened and cooled by passage over the open water but trapped by the strong inversion. As it passed over the ice pack, it must have cooled more at the base, causing a deepening of the cloud. Trajectory analyses indicate that the air in the lowest 1 km was near Barrow, Alaska, ~36 hours earlier. The air was at a temperature of ~9°C over Barrow and was at ~2°C when it reached the *Des Groseilliers* after passage over open water and ice with melt ponds. The cloud mass has a cyclonic appearance in the imagery of Plate 2 and Plate 7 indicating the formation of an organized system underneath the inversion. The origin of clouds like these, which are difficult to detect with standard IR thresholds, is beyond the scope of this paper, but this observation could shed some light on the nature of Arctic cloud systems.

The SHEBA soundings show that during May, more than 90% of the boundary layers had a structure similar to that in Figure 10 where the base of the inversion is elevated. During June, almost half of the inversions begin at the surface like that for 20 July in Figure 10. The number of surface inversions is only 30% during July. The strength of the inversions during June and July may have contributed to the lower-than-normal cloud cover or, possibly, vice versa.

5.6. Near-Infrared Cloud Detection

Summertime Arctic clouds should become easier to detect with future satellite systems because of the availability of near-infrared channels that use wavelengths near 1.6 or 2.1 μm. The new series of AVHRR instruments are designed with a variable channel 3 that can operate at 1.6 or 3.75 μm depending on the solar illumination. Plate 7 shows the 1.6-μm image from the NOAA-15 AVHRR taken 3 hours after the N12 image in Plate 2. The cloud systems are significantly more reflective than either the ice pack or the open water, making identification of the clear areas simpler than has been possible with the AVHRR channels used here. The NOAA-15 1.6-μm channel was only available for a short time before the 3.75-μm channel was turned on permanently. Calibration difficulties and limited temporal coverage excluded its use in this study.

6. Concluding Remarks

On the basis of the comparisons with ground truth data the cloud amounts derived here represent well the cloudiness that occurred over the greater SHEBA domain during the FIRE-ACE period. The determination of detailed subjective thresholds is an essential factor in achieving the good agreement with surface observations. Better objective cloud detection for automated methods like that used by the ISCCP may be accomplished by implementing a BTD threshold that depends on the viewing and illumination angles as well as the surface VIS albedo. Without this, summertime Arctic cloud amounts will be underestimated using VIS, IR, and SI channels only.

The cloud amounts and surface properties observed during FIRE ACE appear to be typical of the conditions in the Arctic during summertime with maximum cloudiness during July. Thus any conclusions drawn from studies of clouds during FIRE ACE should be generally representative of summertime Arctic clouds in this area. Low clouds are the dominant cloud type and their tops will occasionally be warmer than the surface. Mean cloud amount varies diurnally with a peak a few hours before local noon and a range of ~10%. The cloud-top heights derived from the satellite are within a few hundred meters of the radar-determined values for the low clouds. Because no corrections were applied to account for optical depth, the cloud-top heights for clouds above 2000 m are underestimated by 2 km on average. These results, when combined with their concurrent radiative fluxes [*Doelling et al*., this issue], should be valuable for improving the modeling of mesoscale Arctic cloud systems. They can serve as a validation data set providing radiation and cloud products at higher temporal and spatial resolutions than any current Arctic cloud data set. Because the results are also available at the pixel level, the data can be averaged to any type of grid. A comparable data set is being developed for a similar size domain centered on Barrow, Alaska.

The information derived here can also be used to develop improved automated techniques for Arctic cloud detection. Improved scene identification algorithms are being developed to determine (cloud) shadowed or lead pixels. Since leads are often evident in cloudy parts of the VIS image, it may not be necessary to find clear scenes to detect leads. The algorithms applied in this study yield only basic information about the FIRE ACE clouds. Additional research is needed to refine these algorithms for automated application and for deriving other cloud properties, for example, optical depth, phase, and particle size. Still more improvement in Arctic cloud detection will come with the availability of near-infrared sensors on the upcoming AVHRRs and the imagers on the Earth Observing System satellites, Terra and Aqua. With all of those refinements, it will be possible to obtain a more complete picture of clouds and their role in the radiation budget of the Arctic.

Acknowledgments. Special thanks are reserved for Bill Smith Jr., Mandy Khaiyer, Pat Heck, Kirk Ayers, Shalini Mayor, Jeff Otten, and Duane Hazen for monitoring and collecting the data during FIRE ACE. Thanks to David Young and Ash Mahesh for proofing the manuscript and to Yongxiang Hu for his advice on snow modeling. This research was supported by NASA Earth Sciences Enterprise Radiation Sciences Program FIRE Project and by the Environmental

Sciences Division of the U.S. Department of Energy Interagency Agreement DE-AI02-97ER62341 as part of the Atmospheric Radiation Measurement (ARM) Program sponsored by the Office of Science, Office of Biological and Environmental Research, Environmental Sciences Division. The ship data were also obtained from the ARM Program and from the NSF-SHEBA program under agreement OPP-9701730.

References

Chedin, A., N. A. Scott, C. Wachiche, and P. Moulinier, The improved initialized inversion method: A high resolution physical method for temperature retrievals from the TIROS-N series, *J. Clim. Appl. Meteorol*., *24*, 124–143, 1985.

Clothiaux, E. E., T. P. Ackerman, G. G. Mace, K. P. Moran, R. T. Marchaud, M. A. Miller, and B. E. Martner, Objective determination of cloud heights and radar reflectivities using a combination of active remote sensors at the ARM CART sites, *J. Appl. Meteorol*., in press, 1999.

Curry, J. A., W. B. Rossow, D. Randall, and J. L. Schramm, Overview of Arctic cloud and radiation characteristics, *J. Clim*., *9*, 1731–1764, 1996.

Curry, J. A., et al., FIRE Arctic Clouds Experiment, *Bull. Am. Meteorol. Soc*., in press, 2000.

Doelling, D. R., P. Minnis, D. A. Spangenberg, V. Chakrapani, A. Mahesh, S. K. Pope, and F. P. J. Valero, Cloud radiative forcing at the top of the atmosphere during FIRE ACE derived from AVHRR data, *J. Geophys. Res*., this issue.

Dong, X., G. G. Mace, P. Minnis, and D. F. Young, Arctic stratus cloud properties and their impact on the surface radiation budget: Selected cases from FIRE ACE, *J. Geophys. Res*., this issue.

Han, W., K. Stamnes, and D. Lubin, Remote sensing of surface and cloud properties in the Arctic from AVHRR measurements, *J. Appl. Meteorol*., *38*, 989–1011, 1999.

Henderson-Sellers, A., and K. McGuffie, Are cloud amounts estimated from satellite sensor and conventional surface-based observations related?, *Int. J. Remote Sens*., *11*, 543–550, 1990.

Hess, M., P. Koepke, and I. Schult, Optical properties of aerosols and clouds: The software package OPAC, *Bull. Am. Meteorol. Soc*., *79*, 831–844, 1998.

Key, J., and R. G. Barry, Cloud cover analysis with Arctic AVHRR data, 1, Cloud detection, *J. Geophys. Res*., *94*, 18,521–18,535, 1989.

Lazzara, M. A., J. M. Benson, R. J. Fox, D. J. Laitsch, J. P. Rueden, D. A. Santek, D. M. Wade, T. M. Whittaker, and J. T. Young, The Man computer Interactive Data Access System: 25 years of interactive processing, *Bull. Am. Meteorol. Soc*., *80*, 271–274, 1999.

Maslanik, J. A., M. C. Serreze, and T. Agnew, On the record reduction in 1998 western Arctic sea-ice cover, *Geophys. Res. Lett*., *26*, 1905–1908, 1999.

Minnis, P., and E. F. Harrison, Diurnal variability of regional cloud and clear-sky radiative parameters derived from GOES data, part I, Analysis method, *J. Clim. Appl. Meteorol*., *23*, 1032–1052, 1984.

Minnis, P., Y. Takano, and K.-N. Liou, Inference of cirrus cloud properties using satellite-observed visible and infrared radiances, part I, Parameterization of radiance fields, *J. Atmos. Sci*., *50*, 1279–1304, 1993.

Minnis, P., W. L. Smith Jr., D. P. Garber, J. K. Ayers, and D. R. Doelling, Cloud properties derived from GOES-7 for the Spring 1994 ARM Intensive Observing Period using Version 1.0.0 of the ARM satellite data analysis program, *NASA RP 1366*, 59 pp., 1995.

Minnis, P., D. P. Garber, D. F. Young, R. F. Arduini, and Y. Takano, Parameterization of reflectance and effective emittance for satellite remote sensing of cloud properties, *J. Atmos. Sci*., *55*, 3313–3339, 1998.

Nguyen, L., P. Minnis, J. K. Ayers, W. L. Smith Jr., and S. P. Ho, Intercalibration of geostationary and polar satellite data using AVHRR, VIRS, and ATSR-2 data, in *Proceedings AMS 10th Conference Atmospheric Radiation*, pp. 405–408, Am. Meteorol. Soc., Boston, Mass., 1999.

Perovich, D. K., et al., Year on ice gives climate insights, *Eos Trans. AGU*, *80*(41), 481–486, 1999.

Rao, C. R. N., and J. Chen, Post launch calibration of the visible and near-infrared channels of the Advanced Very High Resolution Radiometer on NOAA-14 spacecraft, *Intl. J. Remote Sens*., *17*, 2743–2747, 1996.

Rossow, W. B., and R. A. Schiffer, Advances in understanding clouds from ISCCP, *Bull. Am. Meteorol. Soc*., *80*, 2261–2287, 1999.

Rossow, W. B., A. W. Walker, D. Beuschel, and M. Roiter, International Satellite Cloud Climatology Project (ISCCP): Description of new cloud data sets, *WMO/TD-737*, 115 pp., World Clim. Res. Programme, World Meteorol. Organ., Geneva, 1996.

Schweiger, A. J., R. W. Lindsay, J. R. Key, and J. R. Francis, Arctic clouds in multiyear data sets, *Geophys. Res. Lett*., *26*, 1845–1848, 1999.

Stubenrauch, C. J., W. B. Rossow, F. Cheruy, A. Chedin, and N. A. Scott, Clouds as seen by satellite sounders (3I) and imagers (ISCCP), part I, Evaluation of cloud parameters, *J. Clim*., *12*, 2189–2213, 1999.

Suttles, J. T., R. N. Green, P. Minnis, G. L. Smith, W. F. Staylor, B. A. Wielicki, I. J. Walker, D. F. Young, V. R. Taylor, and L. L. Stowe, Angular radiation models for Earth-atmosphere system, in *Shortwave Radiation*, vol. I, *NASA RP 1184*, 144 pp., 1988.

Warren, D., AVHRR channel-3 noise and methods for its removal, *Int. J. Remote Sens*., *10*, 645–651, 1989.

Warren, S. G., C. J. Hahn, J. London, R. M. Chervin, and R. Jenne, Global distribution of total cloud cover and cloud type amounts over the ocean, *NCAR Tech. Note*, *NCAR TN-317+STR*, Natl. Cent. for Atmos. Res., Boulder, Colo., 1988.

Young, D. Y., P. Minnis, D. R. Doelling, G. G. Gibson, and T. Wong, Temporal interpolation methods for the Clouds and the Earth's Radiant Energy System (CERES) Experiment, *J. Appl. Meteorol*., *37*, 572–590, 1998.

R. F. Arduini, SAIC, Hampton, VA 23666.

V. Chakrapani, D. R. Doelling, R. Palikonda, and D. A. Spangenberg, AS & M Inc., Hampton, VA 23666.

P. Minnis and L. Nguyen, Atmospheric Sciences, NASA Langley Research Center, MS 420, Hampton, VA 23681. (p.minnis@larc.nasa.gov)

M. Shupe, Science and Technology Corporation, Boulder, CO 80303.

T. Uttal, NOAA/ETL, Boulder, CO 80303.

(Received January 7, 2000; revised May 16, 2000;
accepted July 5, 2000.)